Journal of Glaciology

Article

Cite this article: Ruols B, Baron L, Irving J (2023). Development of a drone-based ground-penetrating radar system for efficient and safe 3D and 4D surveying of alpine glaciers. *Journal of Glaciology* **69**(278), 2087–2098. https://doi.org/10.1017/jog.2023.83

Received: 11 May 2023
Revised: 21 September 2023
Accepted: 22 September 2023
First published online: 23 November 2023

Keywords:
Glacier geophysics; Glaciological instruments and methods; Ground-penetrating radar (GPR); Drone; Uncrewed aerial vehicle (UAV)

Corresponding author:
Bastien Ruols; Email: bastien.ruols@unil.ch

cambridge.org/jog

Development of a drone-based ground-penetrating radar system for efficient and safe 3D and 4D surveying of alpine glaciers

Bastien Ruols, Ludovic Baron and James Irving

Institute of Earth Sciences, University of Lausanne, Lausanne, Switzerland

Abstract

Recent research has highlighted the potential for high-resolution, high-density, 3D and 4D ground-penetrating radar (GPR) acquisitions on alpine glaciers. When carried out on foot, such surveys are laborious and time consuming, which limits their application to small domains of limited glaciological interest. Further, crevasses and other hazards make the data acquisition risky. To address these issues, we have developed a drone-based GPR system. The system has a payload weight of 2.2 kg and a data output rate of 14 traces per second. An 80-MHz antenna and a recording time of 2800 ns mean that depths of over 100 m can be reached in temperate ice. Differential GPS positioning assures accurate flight paths. At a speed of 4 m s^{-1} and height of 5 m above the glacier surface, our system can acquire over 4 line-km of GPR data in 20 min on a single set of drone batteries. After presenting the technical specifications of the system and tests required to optimize its performance, we showcase a recently acquired 3D dataset from the Otemma glacier in Switzerland, where 462 parallel GPR profiles were surveyed at a 1-m line spacing, totaling over 112 line-km of data, in only 4 days.

1. Introduction

Thanks to the excellent propagation characteristics of electromagnetic waves in snow and ice, ground-penetrating radar (GPR) has been one of the key geophysical methods used in the field of glaciology for over 50 years (Schroeder and others, 2020, Schroeder, 2022). Initially developed and tested in polar regions (e.g. Harrison, 1970; Jacobel and Anderson, 1987; Bamber, 1989), GPR is now employed regularly on alpine glaciers worldwide to (i) determine ice thickness and estimate ice volume (e.g. Narod and Clarke, 1994; Fountain and Jacobel, 1997; Flowers and Clarke, 1999); (ii) monitor the nature of the glacier bed and identify sedimentary structures (e.g. Arcone and others, 1995; Glasser and others, 2006; King and others, 2008); (iii) identify shear zones and crevasses (e.g. Goodsell and others, 2002; Nobes and others, 2005; Bradford and others, 2013); (iv) map internal water bodies and subglacial lakes (e.g. Vincent and others, 2012; Garambois and others, 2016; Rutishauser and others, 2022); (v) estimate ice water content (e.g. Pettersson and others, 2004; Murray and others, 2007; Bradford and others, 2009); (vi) distinguish between cold and temperate ice (e.g. Brown and others, 2009; Eisen and others, 2009; Bælum and Benn, 2011); (viii) identify and characterize englacial and subglacial channels (e.g. Sharp and others, 1993; Moorman and Michel, 2000; Kulessa and others, 2008); and (viii) study glacier surge mechanisms (e.g. Jacobel and Raymond, 1984; Murray and others, 2000; Woodward and others, 2003).

Typically, GPR surveys conducted on glaciers have involved the acquisition of data over one or a small number of profile lines (e.g. Farinotti and others, 2009; Harper and others, 2010; Urbini and others, 2017), thus providing a 2D transect view of the englacial and subglacial conditions. Over the past decade, an increasing number of researchers have carried out so-called 3D GPR surveys in alpine glaciological environments, where data are acquired over a series of regularly spaced parallel survey lines to gain further detailed information about the internal structure of the ice and/or bed geometry (e.g. Saintenoy and others, 2013; Langhammer and others, 2019b; Egli and others, 2021a). In this regard, both ice-based (e.g. Binder and others, 2009; Saintenoy and others, 2011; Del Gobbo and others, 2016) and helicopter-based (e.g. Merz and others, 2015; Rutishauser and others, 2016; Grab and others, 2018) 3D GPR surveys have been conducted. On one hand, ice-based surveys allow for the acquisition of high-density and high-resolution 3D GPR data and have proven to be a valuable tool for the study of, for instance, englacial and subglacial hydrology (Church and others, 2019; Church and others, 2021; Egli and others, 2021a). However, the corresponding data acquisitions are labor intensive and slow to carry out, and the surveyed areas are consequently limited in size. Such surveys may also be dangerous due to surface features such as crevasses and moulins, or even impossible in regions of the glacier that are inaccessible. Helicopter-based surveys, on the other hand, permit the coverage of larger areas (e.g. Arcone and Yankielun, 2000). However, in addition to being expensive and polluting, they come at the cost of reduced resolution of internal glacier structures as the GPR antennas are located much further from the ice surface. Further, helicopter-based survey lines cannot be flown with a spacing on the order of the dominant GPR wavelength in order to provide high-density measurements.

https://doi.org/10.1017/jog.2023.83 Published online by Cambridge University Press

Repeated 3D GPR acquisitions over the same area, otherwise known as 4D surveys, are even less common in glaciological settings. Indeed, with such acquisitions, the above-listed drawbacks become even more determinant and there exists the additional challenge of returning to the glacier on a regular basis to record 3D GPR data in the same spatial locations. Nonetheless, previous initial work has suggested that time-lapse GPR measurements on glaciers may be valuable. Irvine-Fynn and others (2006), for example, examined the hydrothermal dynamism within a polythermal glacier during a single ablation season and showed that the ice water content varies in response to an evolving englacial and subglacial drainage system. Church and others (2020) mapped the spatial extent of a dynamic englacial conduit network on a temperate glacier multiple times over a two-year period, which provided insight into the evolution of the glacier hydrological system. Finally, Mingo and others (2020) detected changes in englacial water storage using time-lapse GPR surveys, which led to a better understanding of englacial lake filling and drainage cycles. All of this research leads us to expect that recording frequent high-resolution and high-density repeated 3D GPR data on glaciers would provide new and important insights into glacier temporal dynamics. At the present time, however, a means of acquiring such data over relevant areas of interest and reasonable time frames does not exist.

In recent years, numerous advances in uncrewed aerial vehicle (UAV) or drone technology have opened new and exciting data acquisition possibilities in the field of geophysics. Indeed, a wide variety of geophysical instruments have been deployed on drone-based platforms, which include: (i) electromagnetics (e.g. Stoll and others, 2019; Parshin and others, 2021; Kotowski and others, 2022), (ii) magnetics (e.g. Døssing and others, 2021; Kolster and Døssing, 2021; Walter and others, 2021), (iii) gamma-ray (e.g. van der Veeke and others, 2021a; van der Veeke and others, 2021b; Kunze and others, 2022), (iv) gravity (e.g. Weiner and others, 2020; Luo and others, 2022), (v) lidar (e.g. Lin and others, 2019; Yin and Wang, 2019; Tao and others, 2022), (vi) sonar (e.g. Dietrich, 2017; Bandini and others, 2018; Koutalakis and Zaimes, 2022) and (vii) radar instruments. Initial drone-based radar systems involved small, lightweight antennas, first operating in the Ka-band (24–40 GHz) (Weiss and others, 2005), followed by the X-band (8–12 GHz) and C-band (4–8 GHz) (Zaugg and others, 2010; Remy and others, 2012; Aguasca and others, 2013). These systems proved that radar imaging using UAVs is feasible but were not suitable for subsurface investigations due to the limited penetration into the ground. Subsequent systems permitted operation at lower frequencies and were sufficiently advanced to be used in the context of (i) landmine detection (Burr and others, 2018; Fernandez and others, 2018; Dill and others, 2019); (ii) archeological exploration (Yarleque and others, 2017); (iii) snow cover investigation (Jenssen and others, 2020; Jenssen and Jacobsen, 2020); (iv) soil moisture mapping (Wu and others, 2019); (v) snow hydrology (Valence and others, 2022); and (vi) avalanche rescue (SPH Engineering). An excellent review of the state-of-the-art of contactless GPR imaging, specifically with regard to UAV-borne GPR, is presented in Catapano and others (2022). In all of the above cases, however, the developed GPR systems involved antenna frequencies ranging from 500 MHz to 4 GHz which still do not allow for sufficient penetration into a glacier. To our knowledge, a drone-based GPR instrument operating at lower frequencies, with the specific objective of investigating internal glacier structures in detail, has not yet been presented.

In this paper, we introduce a newly developed drone-based, impulse GPR system that has been designed for the specific purpose of conducting high-density 3D and 4D surveys on alpine glaciers in a safe and highly efficient manner, thereby combining the advantages and minimizing the disadvantages of ice-based and helicopter-based surveys. The system takes advantage of modern real-time-sampling GPR technology with a high number of stacks, which permits the rapid collection of high-resolution data. A single custom-made transmit–receive antenna, operating at a center-frequency of 80 MHz, along with carbon-fiber supports ensure a minimal payload weight, thus maximizing flight time on a single set of batteries. Drone flight localization using dGPS technology permits the precise following of parallel survey lines, which is essential for the acquisition of high-quality 3D and 4D data. We first outline below the drone-based GPR system and data acquisition methodology. Next, we describe a series of flight parameter tests performed to optimize the system stability and quality of the measurements. Finally, to illustrate the potential for drone-based GPR on glaciers to acquire large high-density and high-resolution 3D data, we present a recently recorded dataset from the Otemma glacier, Switzerland.

2. The drone-based GPR system

2.1. Construction and specifications

Our drone-based GPR system is divided into four different units (Fig. 1). The Drone Unit is comprised of an M300 RTK drone manufactured by Shenzhen DJI Sciences and Technologies (China) along with the True Terrain Following (TTF) navigation system developed by SPH Engineering (Latvia). The GPR Unit contains a GPR controller, which was custom designed to our specifications by Utsi Electronics Ltd. (UK), and a homemade single transmit–receive antenna, both of which are connected to the Drone Unit using custom designed 3D printed parts. The Operator Unit is composed of a field computer, a mobile phone, as well as a remote controller for the drone. Finally, the dGPS Unit consists of the D-RTK 2 high-precision global navigation satellite system (GNSS) mobile station from DJI.

The M300 drone, when used in real time kinematic (RTK) mode with the D-RTK 2 base station, has a navigational positioning accuracy of approximately 1 cm horizontally and 2 cm vertically thanks to real-time differential GPS corrections. When combined with the TTF system, which is composed of an onboard computer and a 24-GHz radar altimeter, it can correct its elevation as it flies with the aim of keeping an approximately constant height above the glacier surface. This function is particularly important in areas where the surface topography is highly variable in the sense that we wish to fly as close to the glacier as practically possible in order to optimize the resolution of the GPR data. Flight parameters, such as the desired height of the drone above the surface or the maximum descent speed, are set via an internal configuration file. Additionally, GPS data are output from the drone to the GPR controller such that each GPR trace is tagged with its exact time and position. All flight data, including the drone speed, flight dynamics parameters (i.e. pitch, roll and yaw angles), dGPS positions and RTK status, are logged while the system is in operation.

The GPR controller is responsible for both generating the radar pulse that is sent into the antenna and recording the pulses that are reflected from heterogeneities within the ice. Sampling of the recorded waveform is done in real time, meaning that each GPR trace is recorded all-at-once rather than through a series of interleaved samples. Each trace is thus stored rapidly, which means that many stacks are possible and that a high signal-to-noise ratio can be achieved. Indeed, our GPR controller records 24-bit traces over a time range of 2800 ns, corresponding to a survey depth of more than 200 m in glacier ice, with a temporal sampling interval of 3.125 ns. The trace acquisition rate is approximately 14 Hz and each raw measurement is stacked

https://doi.org/10.1017/jog.2023.83 Published online by Cambridge University Press

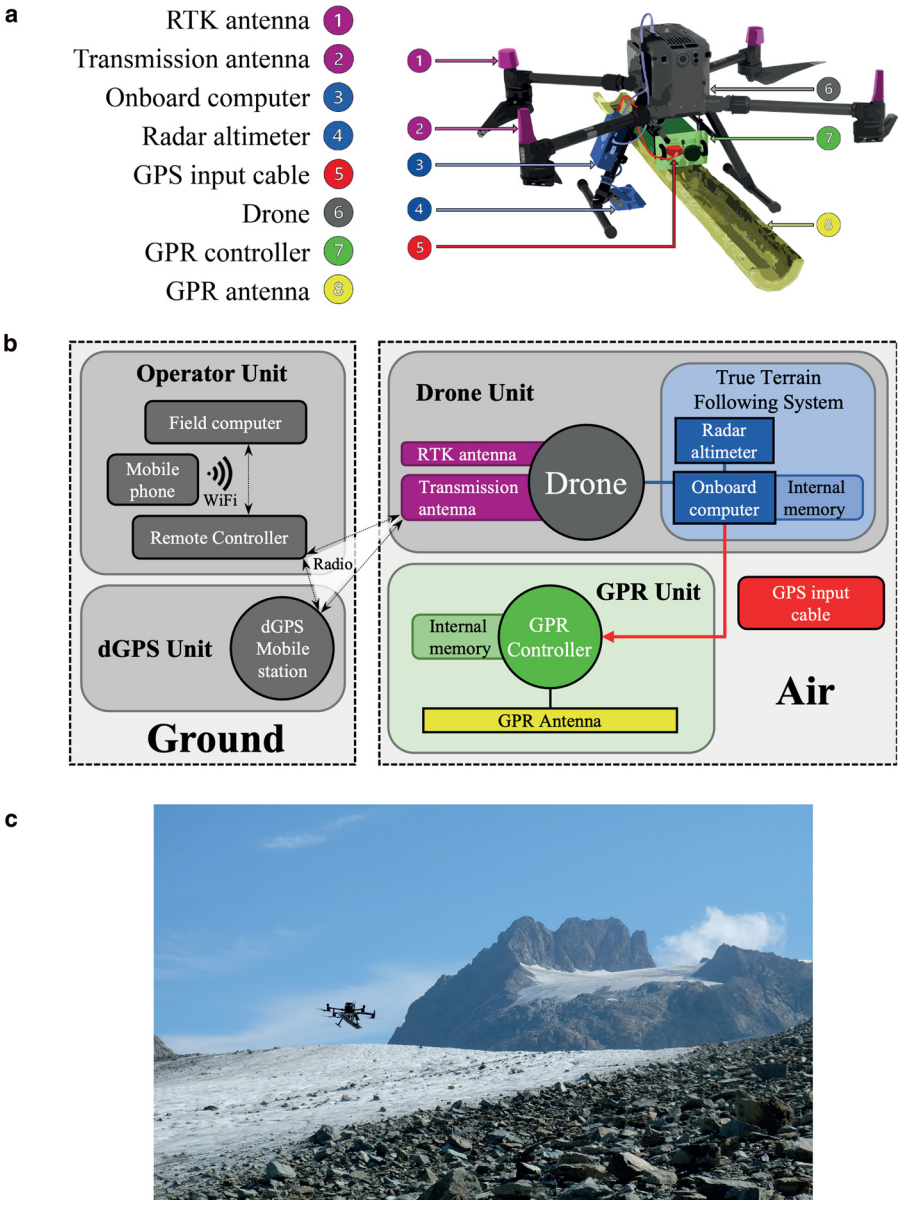

Figure 1. Drone-based GPR system: (a) illustration of the system components; (b) diagram showing the structure and interactions between the devices; (c) photo of the system operating over the Otemma glacier in August 2022.

roughly 5000 times, resulting in an expected 70-fold improvement of signal-to-noise. When flying the drone at a speed of 4 m s^{-1}, we are able to record more than three GPR traces per meter, which allows for high-quality along-profile data. Our custom-built lightweight unshielded GPR antenna, used in monostatic mode, is a resistively loaded butterfly dipole having a center frequency of approximately 80 MHz and an effective bandwidth of 120 MHz. With this antenna, we have found that we can typically image to well over 100 m depth in temperate alpine glaciers, even in regions where substantial rock debris is present on the glacier surface. Finally, GPS NMEA sentences are logged by the GPR controller at a rate of 5 Hz such that the position of each GPR trace can be precisely determined. Data are recorded onto an SD card located on the controller in order to avoid interference with the radio command. Recording of GPR data begins immediately when the system is turned on.

Table 1 summarizes the specifications of the different components of the drone-based GPR system along with their weights. The total payload of the system is approximately 2.2 kg, which is well below the 2.7 kg payload capacity of the M300 drone. According to the manufacturer, the flight time of the M300 on a single set of batteries with such a payload should be approximately 34 min. However, this is highly variable and depends not only on the survey conditions (e.g. air temperature, pressure, wind speed), but also on the flight parameters discussed in Section 3.1.

Table 1. Drone GPR system specifications

System component	Specification	Magnitude
GPR controller	Trace length	2800 ns
	Temporal sampling interval	3.125 ns
	Trace acquisition rate	14 Hz
	Number of stacks	~5000
	Weight	1460 g
Drone	Navigational precision	~1 cm horizontal ~2 cm vertical
	Weight	6300 g
	Maximum payload weight	2700 g
TTF system	Radar altimeter accuracy	~2 cm
	Radar altimeter acquisition rate	2 Hz
	Weight	410 g
Transmit–receive antenna	Center frequency	80 MHz
	Effective bandwidth	120 MHz
	Length	130 cm
	Weight	250 g

https://doi.org/10.1017/jog.2023.83 Published online by Cambridge University Press

2.2. Survey methodology

The first step in conducting a drone-based GPR survey is planning the flight mission. This is done either in advance at the office, or on-site in the field, and is accomplished using the Universal ground Control Software (UgCS) software from SPH Engineering. To this end, we use the so-called Area Scan tool to define a series of parallel survey lines over the region of interest. This involves choosing the desired orientation of the lines, the orientation of the drone, the line spacing and the flight speed. With this information, the software then programs a succession of waypoints to which the aircraft will fly in chronological order.

After planning the flight mission, its feasibility is verified using a smaller and cheaper 'crash drone' before conducting the final 3D GPR survey. Indeed, even if the M300 drone has anticollision sensors on all sides, highly variable topography including a rough glacier surface, steep valley walls, lateral and medial moraines, and the presence of large boulders represents a difficult flight environment, and all efforts are made to ensure that a crash with expensive geophysical equipment is avoided. Further, the survey environment may change during a 4D survey, in the sense that glacier melt between acqusitions may put the boundaries of the GPR grid closer to valley walls than in previous surveys. As the smaller drone will not have the battery capacity to fly the entire grid, a second mission is created whose primary purpose is to check the edges of the survey domain as well as any visibly challenging regions in its interior. We have found this strategy to be sufficient to ensure the safety of the system.

Once the flight mission has been correctly programmed, the D-RTK 2 base station is configured. When considering 4D GPR surveys and to ensure the best possible mission repeatability in terms of positioning, the base station should be placed at the same location for each acquisition. The mission is next uploaded to the remote controller, and the TTF mode is activated using a second software, the UgCS Custom Payload Monitor (CPM). Once the mission has started, the drone moves toward the first waypoint of the trajectory, orients itself as programmed, and begins to fly along the first profile. Because the flight missions are generally significantly longer than what the system can cover using a single set of drone batteries, the batteries must be changed during the survey. In this regard, when the batteries reach a critically low level (minimum 20%), the mission is paused and the drone is landed manually. After changing the batteries, the mission is uploaded again from the last waypoint reached in the previous flight and the data acquisition is resumed. In the common case where the drone needs to be flown back to the operator because its location on the glacier is difficult to access, the mission must be stopped earlier to dedicate battery power to that task.

3. Flight parameters and testing

In the following we explore the effects of various flight parameters for the drone-based GPR system with the aim of optimizing its performance. We first consider different types of turns and mission trajectories and their impact on the flight path, drone battery consumption and survey logistics. We then address the choice of profile line spacing for 3D and 4D alpine glacier surveys. Next, we examine the effect of the chosen flight speed and height above the glacier surface on survey logistics and GPR data quality. Finally, we assess the stability of the system during data acquisition.

3.1. Turns and trajectories

The UgCS software proposes two options for turning the drone after the completion of each profile line: the Stop & Turn (S&T) and the Adaptive Bank Turn (ABT) (Fig. 2). With the S&T option, the drone flies directly to each waypoint, stops, and then moves towards the next waypoint. In this manner, the turns are abrupt. Conversely, with the ABT option, the system considers that it has reached a particular waypoint when it comes within a prescribed acceptance radius. It begins moving towards the next waypoint without stopping its motion, and in this manner the turns are smooth. Both types of turns were tested to assess their impact on the quality of the resulting flight paths and on the battery consumption. To this end, a flight trajectory comprised of twenty-six, 105-m-long profile lines, laterally spaced by 2 m, was programmed and flown at a specified speed of 3 m s^{-1}. The profiles were flown in sequential order from one side of the grid to the other. Figures 3a and b show the path taken by the drone and the measured flight speed using the S&T and ABT options, respectively. As expected, we see that the S&T option results in straighter flight lines, whereas the ABT option results in slight deviations from the scheduled trajectory when starting a new profile. Further, the flight speed along each profile line is more uniform using S&T turns which translates into a more constant GPR trace acquisition rate in distance. The drone battery consumption during the S&T test, however, was found to be 64%, whereas it was 41% for the ABT test, which represents a 23% difference. Battery life being most critical in our case, it was decided to always use the ABT option with the drone-based GPR system. Issues related to variable drone speed along the GPR survey lines and slight deviations from the programmed path are indeed relatively minor and can be addressed by careful binning of the data (see Section 4.3).

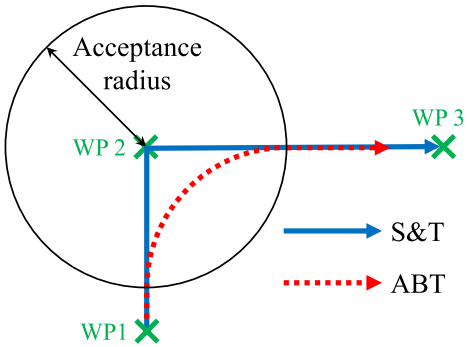

Figure 2. Two types of turns available with the UgCS software. S&T: Stop & Turn. ABT: Adaptive Bank Turn. WP: Waypoint.

Even when using the ABT option, the drone still needs to decelerate and accelerate strongly when moving from one profile to the next, and an important part of its battery consumption is dedicated to these transitions. To mitigate this issue, one might consider modification of the flight trajectory in order to increase the turn radius at the expense of not flying the profiles in sequential order. The latter is common in marine bathymetry surveys where it is not possible to make sharp turns (e.g. Kurowski and others, 2019). To investigate this possibility, we considered an alternate ABT trajectory consisting of sequentially flying all odd-numbered profiles to the end of the survey grid, followed by flying the even-numbered profiles in reverse order on the way back. Figure 3c shows the resulting variations drone position and speed, which are seen to be not significantly different from those corresponding to the trajectory presented in Figure 3b. Surprisingly, we also found that there was no meaningful difference in battery consumption between the alternate trajectory (40%) and the previously considered one (41%). The main potential advantage when using the alternate trajectory is that the starting and ending locations of the flights are on the same corner of the grid, which may serve useful in areas where the glacier is difficult to access because most of the drone battery power can be used for data acquisition, and not for reaching the starting or

https://doi.org/10.1017/jog.2023.83 Published online by Cambridge University Press

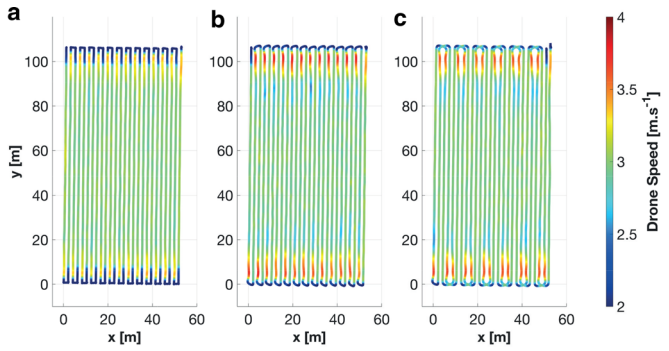

Figure 3. Drone position and speed for two types of turns and trajectories: (a) Stop & Turn option for a trajectory where the GPR profile lines are flown in sequential order (drone battery consumption 64%); (b) Adaptive Bank Turn option for the same trajectory as in (a) (drone battery consumption 41%); (c) Adaptive Bank Turn option for a trajectory where the odd-numbered profiles are flown first in sequential order, followed by the even-numbered profiles in reverse order (drone battery consumption 40%). The programmed drone speed was 3 m s^{-1}.

ending location of the grid. The choice between the two types of trajectories should therefore be based on the field site.

3.2. Survey line spacing

To avoid the spatial aliasing of dipping diffraction tails and steeply dipping reflectors, it is generally recommended that GPR data are acquired with a trace spacing that is no greater than 25% of the dominant antenna wavelength in the studied medium (Grasmueck and others, 2005). Our GPR antenna has a center-frequency of roughly 80 MHz, which corresponds to a so-called 'quarter-wavelength' spacing of approximately 50 cm in glacier ice. When surveying in the along-profile direction, as the trace acquisition rate of our GPR controller is 14 Hz, there is no problem to respect this criterion for flight speeds of up to 7 m s^{-1}. In the context of 3D surveys and in the across-profile direction, however, it poses a logistical challenge because acquiring data with such a line spacing would prohibit the coverage of large areas in a reasonable time frame. For this reason, we generally set the line spacing for our 3D drone-based glacier surveys to 1 m, which corresponds to roughly 48% of the dominant antenna wavelength in ice. We have found this choice to represent an acceptable balance between data quality and coverage, and it is fully consistent with other studies. Indeed, recent 3D GPR work on glaciers considered line spacings at 42% and 83% (Egli and others, 2021a) and 30% (Church and others, 2021) of the dominant antenna wavelength. The corresponding data from these two studies were of exceptionally high quality and provided important information on the englacial and subglacial hydrology of the studied glaciers.

3.3. Flight altitude and speed

The aim of the TTF mode is to correct the altitude of the drone as it flies in order to keep a roughly constant height above the glacier surface. In this regard, there are a number of important practical details that must be considered when choosing the desired flight altitude and speed for a drone-based GPR survey. First, we have found there to be an approximately 1-s delay between the measurements of the system radar altimeter, which are used to determine the altitude correction, and the time at which the actual correction takes place. Depending on the glacier surface topography, this can pose severe problems of the drone is flown too low and/or too fast. As an example, Figure 4 shows the position of our drone-based GPR system relative to the glacier surface along four consecutive profiles acquired at the Otemma glacier (Switzerland) during the summer of 2022. The profiles were flown at a speed of 4 m s^{-1} and the desired height above the glacier surface was set to 5 m. On Figure 4, odd-numbered profiles were flown from south to north, whereas even-numbered ones were flown from north to south. Between 300 m and 340 m position, we see that the glacier surface rises and then falls by approximately 5 m due to the presence of a lateral moraine. The drone can be seen to correct its altitude to account for this feature, but the corrections are delayed such that there is a significant horizontal offset between the drone's position and the surface topography, in this case approximately 5 m. Had the drone been flown lower and/or faster, a crash may have occurred. On one hand, flying close to the glacier surface allows for better antenna-ice coupling and limits the influence of the layer of air between the antennas and the glacier on the GPR data, which should in theory improve the data quality. However, a slow flight speed must be selected in this case, which can severely limit the acquisition rate. On the other hand, flying higher means that faster drone speeds can be considered with minimal risk of crashing. In this case, however, less energy from the antennas will be transmitted into the ice and the presence of the air layer must be taken into account in the data processing. Indeed, the assumption of a constant velocity medium, as is typically done in surface-based glaciological GPR studies (e.g. Church and others, 2020; Church and others, 2021; Egli and others, 2021a), cannot be made because the moveout of near-surface scatterers will be affected by the air (Booth and Koylass, 2022), and a spatially variable velocity model must be used to image the data (e.g. Grab and others, 2018; Langhammer and others, 2019a).

To practically investigate the latter aspects, we flew the same cross-glacier profile multiple times with our drone-based GPR system at heights ranging from 1 m to 9 m, all using a flight speed of 1 m s^{-1}. Four of the resulting GPR profiles are shown in Figure 5, where only basic data processing consisting of mean trace removal and de-wow filter was applied. At first glance, the nine profiles appear to be similar. The reflection from the glacier bed (blue rectangle) is clearly visible in all cases and there does not appear to be a strong difference in data quality between 1 m and 9 m flight altitude, as might have been expected from antenna coupling arguments. Focusing on the internal glacier reflections (yellow rectangle), we similarly see that there is no clear difference in data quality, in the sense that the same events appear to be present in each dataset with roughly equal strength. When focusing on a single diffraction hyperbola in the upper part of the section (red ellipse), however, we do see that increasing the drone height affects the diffraction moveout, in that the diffraction tails become less steep because of refractions at the air-ice interface (Booth and Koylass, 2022). Based on these results, we can state that flying higher above the glacier surface, even if it does distort shallow events, does not result in a significantly lower quality GPR dataset. For this reason, and to balance data quality and coverage, we made the choice to fly at a height of 5 m above the glacier surface and at a speed of 4 m s^{-1} for our 3D and 4D work. With these parameters and considering ABT turns, we have found that the effective flight time of our drone-based GPR system, operating between elevations of 2100 and 2800 m above sea level, is approximately 19 min on a single set of batteries. This translates into approximately 4 line-km of GPR data per set of batteries.

One final item requiring discussion with regard to drone height and speed is the presence of large crevasses or moulins, which represent sharp and significant drops in the glacier surface topography. When the drone is flying above such features, it will try to lower its altitude to stay at the programmed height above the surface, and thus there is a considerable risk of crashing into the ice. To mitigate this risk, care should be taken when setting the minimum and maximum height measurements to be

https://doi.org/10.1017/jog.2023.83 Published online by Cambridge University Press

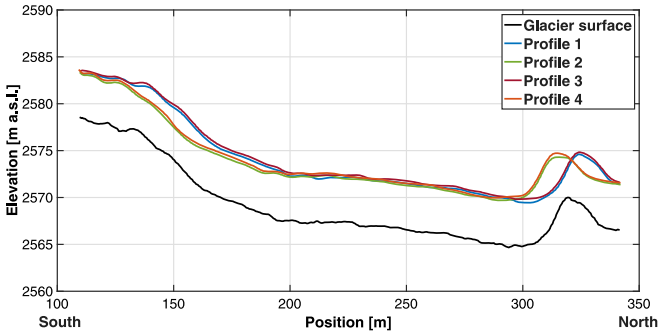

Figure 4. Measured elevation of the drone-based GPR system above the glacier surface along four consecutive profiles taken from a 3D GPR dataset recorded on the Otemma glacier in the summer of 2022. Profiles 1 and 3 were flown from south to north, whereas profiles 2 and 4 were flown from north to south. The drone was programmed to have a flight speed of 4 m s^{-1} and desired height above the glacier surface of 5 m.

accepted from the radar altimeter. If it happens that the altimeter records a value outside of this range, the drone will instantaneously stop its horizontal motion and rise vertically by a few meters. This solution works well in the case where the height of the drone above the surface faces an abrupt change, but it has limited performance for long crevasses aligned with the direction of the drone. In the latter case, the maximum descent speed of the drone should be carefully chosen to limit the risk of crash and provide additional time for the operator to pause the data acquisition when necessary. In any case, it is critical that the operator keeps constant watch over the system with the ability to manually take control at any moment, in order to bypass such obstacles and resume automatic control afterwards.

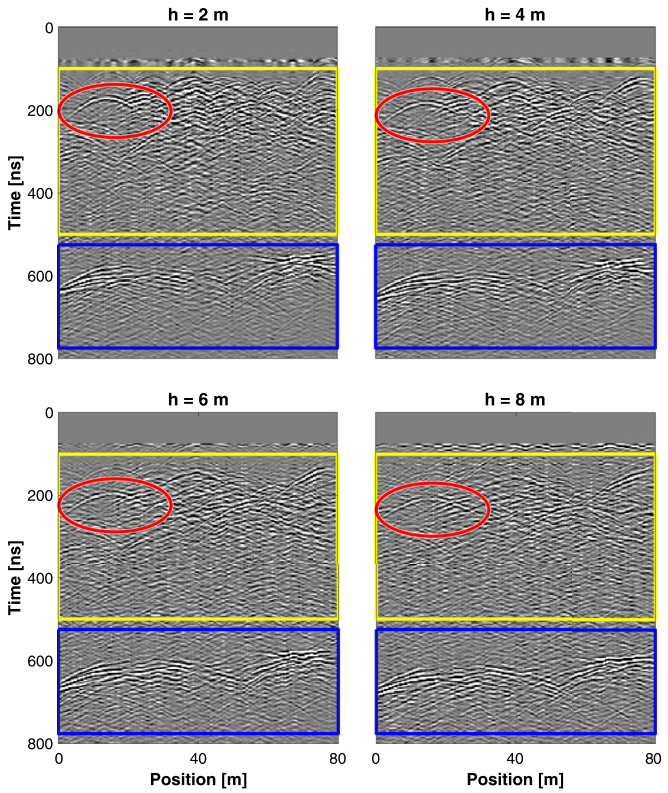

Figure 5. Impact of drone height above the glacier surface. The same cross-glacier profile at the Otemma glacier was flown nine times at different heights ranging from 1 m to 9 m. The GPR data obtained at heights of 2 m, 4 m, 6 m and 8 m are shown. Only mean trace removal and de-wow have been applied. The programmed drone speed was 1 m s^{-1}. The blue rectangle highlights the ice-bedrock reflection, whereas the yellow rectangle highlights the zone containing internal glacier reflections and scattered energy. A single diffraction hyperbola is highlighted using the red ellipse.

3.4. Drone orientation and stability

It has been previously shown that multi-component GPR surveys involving two orthogonal antenna orientations have strong advantages for glaciological and other studies in the sense that directional effects of the antenna radiation patterns can be strongly reduced, and the corresponding data can be used to create a pseudo-scalar wavefield (Lehmann and others, 2000; Langhammer and others, 2017). Such surveys, however, are time-consuming and labor-intensive when the orthogonal orientations cannot be collected simultaneously, and for this reason the vast majority of glacier GPR data are acquired using a single antenna orientation (e.g. Church and others, 2019, 2021; Egli and others, 2021a). For best results, the antenna dipole should be oriented parallel to the ice flow direction to allow for stronger and more coherent bedrock reflections (Langhammer and others, 2017). According to the construction of our system (Fig. 1a), this means the drone should be oriented such that it is facing either up- or down-glacier. For our 3D and 4D work, we decided to always orient the drone such that it is facing up-glacier (Fig. 6a). Parallel survey lines are run in an across-glacier direction, perpendicular to ice flow.

To evaluate the stability of our system during flight, we now examine the three flight dynamics parameters (yaw, pitch and roll), which are illustrated in Figure 6b. Indeed, even if the drone-based GPR system appears to be visually highly stable during operation, these parameters will vary due to its motion. Figure 7 shows these flight dynamics parameters over ten consecutive profiles from a 3D dataset. The profiles were flown in alternating directions using ABT turns. The programmed drone speed was 4 m s^{-1}. We see that the pitch angle stays close to zero along the profiles, whereas the roll angle alternates from positive to negative values from one profile to another because the antenna position falls slightly behind the drone body during flight. The mean absolute amplitude of the roll angle along the profiles is below 5 degrees, which results in a translation in the location of the GPR antenna of 2.5 cm horizontally and 0.1 cm vertically. These shifts are afterwards corrected when determining the GPS coordinates of the antenna during processing (see Section 4.3). Finally, the yaw angle, relative to the programmed antenna orientation along the flight line, also stays close to zero, further confirming the stability of our system.

4. Example dataset

To highlight the capabilities of our system and the strong potential for drone-based GPR surveying in glaciological studies, we present in this section an example 3D dataset acquired at the Otemma Glacier (Switzerland) in the summer of 2022. Note that our discussion below focuses on the acquisition of the data and on their basic editing and processing in order to obtain a high-quality GPR volume in time. Full details pertaining to depth imaging of the data and their glaciological interpretation are not explored in this paper.

4.1. Field site

The Otemma glacier is a temperate valley glacier located in the Canton of Valais in Southwestern Switzerland (Fig. 8a). It is approximately 7 km long, 600 m wide, and ranges from 2550 to 3790 m elevation. The glacier experienced an average retreat of 32 m per year between 1973 and 2010 (ETHZ VAW, EKK/SCNAT, 2010), and the average ice thickness in 2014 was estimated to be approximately 250 m (Rutishauser and others,

https://doi.org/10.1017/jog.2023.83 Published online by Cambridge University Press

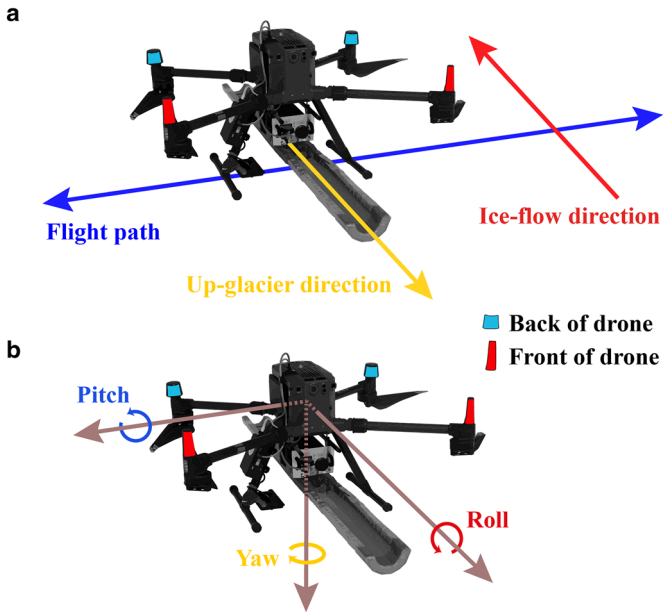

Figure 6. (a) Orientation of the drone-based GPR system during a survey. The front of the drone (red markers) always faces up-glacier, whereas survey lines are flown perpendicular to this direction across the glacier. (b) Illustration of the three flight dynamics parameters.

2016). In 2017, a high-density GPR dataset of size ~200 m × 100 m was acquired on foot in the area close to the glacier snout, which allowed mapping of a major and highly sinuous subglacial channel (Egli and others, 2021a). In the summer of 2018, a large collapse event occurred in the location of the previous GPR survey, which was attributed to the effects of surface ablation combined with melting and block caving inside the channel resulting from the entry of warm air at atmospheric pressure (Egli and others, 2021b). At the time of writing, most of the Otemma glacier is located below the equilibrium line altitude which makes it highly sensitive to increases in average air temperature.

4.2. Data acquisition

Over the course of four days in August 2022, we recorded a large, high-density, high-resolution, 3D GPR dataset near the Otemma glacier snout with the newly developed drone-based system. To this end, a generator was brought to the glacier so that the drone batteries could be charged directly on-site during acquisition, thereby permitting more profile lines to be surveyed per day than our four sets of batteries would normally allow. The first GPR profile was set to be as close to the glacier snout as possible, and subsequent profiles were surveyed moving up-glacier with a line spacing of 1 m. A grid of 462 parallel profiles of length ranging from 140 to 330 m was surveyed, representing a total of more

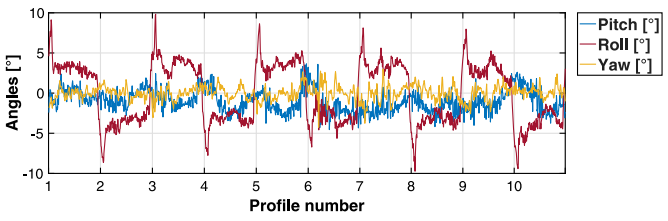

Figure 7. Flight dynamics parameters of the drone-based GPR system over ten consecutive profiles, flown in alternating directions using ABT turns, from a 3D GPR dataset recorded on the Otemma glacier. The programmed drone speed was 4 m s^{-1}. The pitch and roll angles are defined in Figure 6b, whereas the yaw angle is relative to the programmed antenna orientation along the flight line.

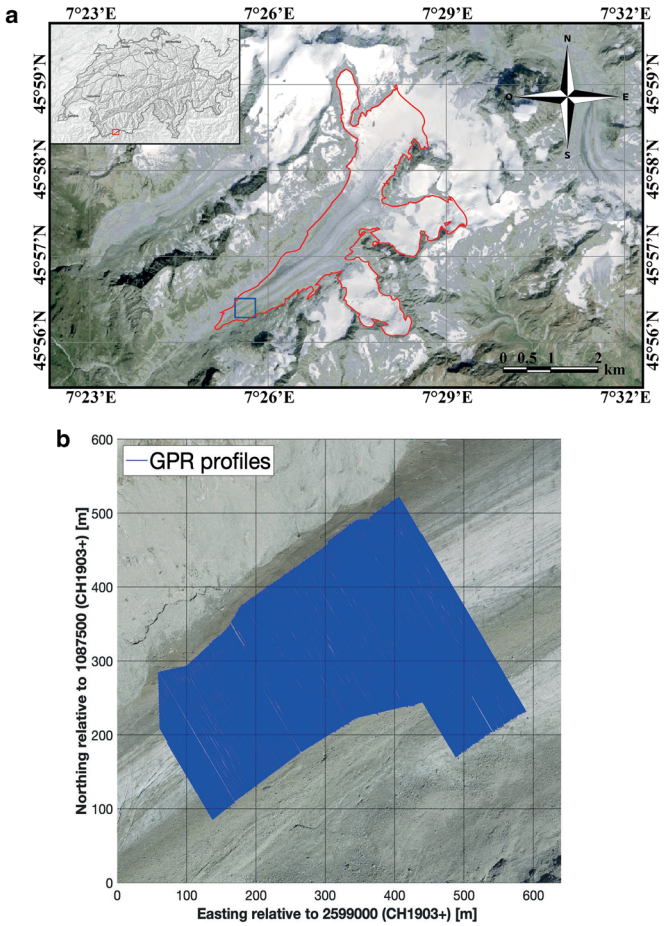

Figure 8. (a) Location of the Otemma glacier (red outline) in southwestern Switzerland (inset). The blue square in the lower ablation zone indicates the region of our GPR survey, which is shown in detail in (b). Profile lines were flown along a southeast-northwest orientation moving up-glacier. Satellite background image in (a) from the Sentinel-2 Mosaic program (NPOC 2020). Inset map in (a) and satellite background image in (b) from the Swiss Federal Office of Topography (Swisstopo).

than 112 line-km of GPR data (Fig. 8b). The approximate area of the grid is 110 000 m^2. The drone was programmed to fly at a speed of 4 m s^{-1} and a height above the glacier surface of 5 m.

4.3. Data editing and processing

Because the GPR trace acquisition rate of our system (14 Hz) differs from the frequency at which GPS data are logged by the GPR controller (5 Hz), interpolation was first performed such that each individual GPR trace could be tagged with precise GPS coordinates. Next, a correction was made to translate these coordinates, which correspond to the location of the RTK antenna, to the location of the center of the GPR antenna (Fig. 1a). To this end, the static offset between the two antennas along with the pitch and roll angles (Fig. 6b) are required. Binning of the GPR data was subsequently performed to create a regular grid of GPR measurements having an inline spacing of 0.4 m and a crossline spacing of 1 m. Thanks to the navigational precision of the drone and thus the limited deviation between the true and programmed coordinates, each GPR profile could be binned independently. This was done by populating each bin with the nearest GPR trace and discarding all other traces, which we have found to provide a cleaner result than averaging over multiple nearby recordings.

Only basic processing of the Otemma 3D GPR dataset was carried out to produce the results presented in this paper. This consisted of the following series of steps, which were performed using customized codes in MATLAB:

https://doi.org/10.1017/jog.2023.83 Published online by Cambridge University Press

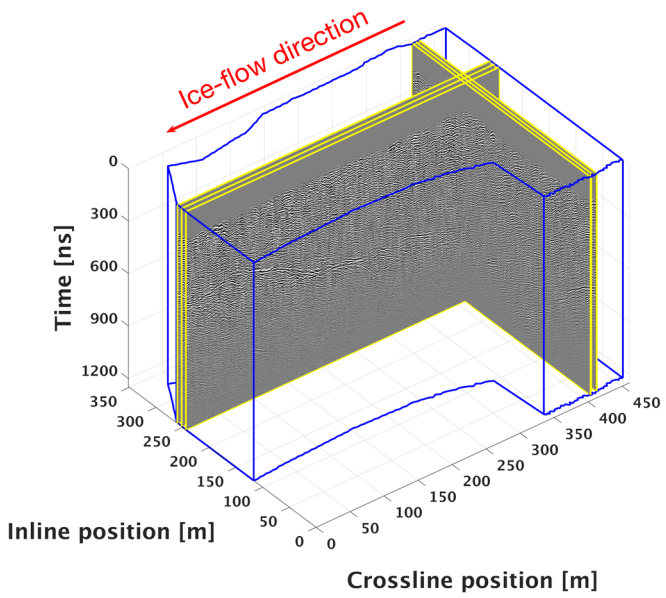

Figure 9. 3D representation of the Otemma GPR dataset as a 'data cube', and the location of the three inline and crossline profiles displayed in Figures 10 and 11. The blue outline shows the boundaries of the data volume. The GPR profiles were surveyed perpendicular to the ice flow direction.

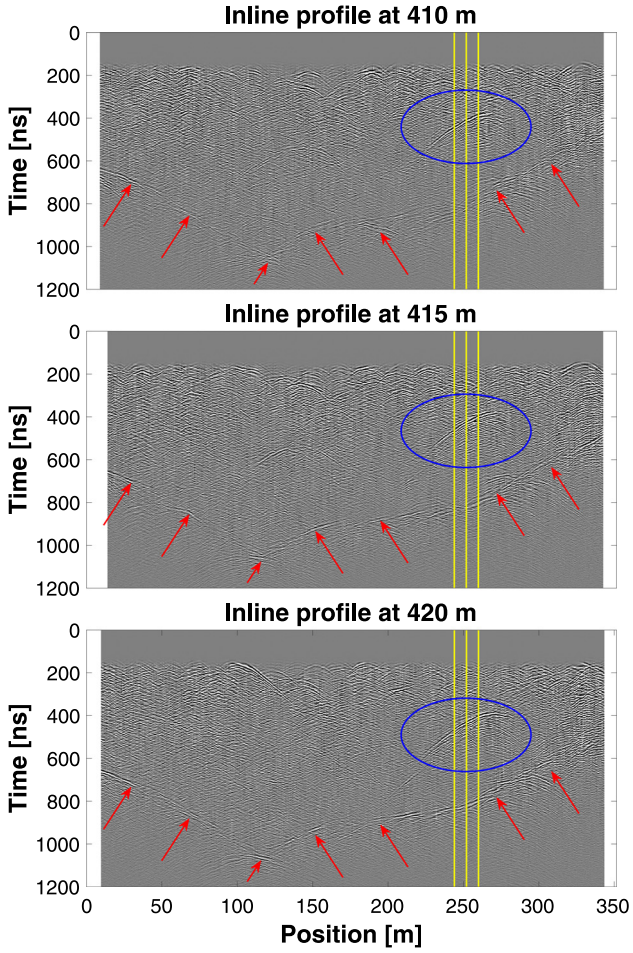

Figure 10. Example inline GPR profiles. Three profiles separated by 5 m are depicted. The glacier bed is clearly visible (red arrows), and a large englacial feature can be seen (blue ellipse). The yellow lines denote the intersections with the three crossline profiles shown in Figure 11.

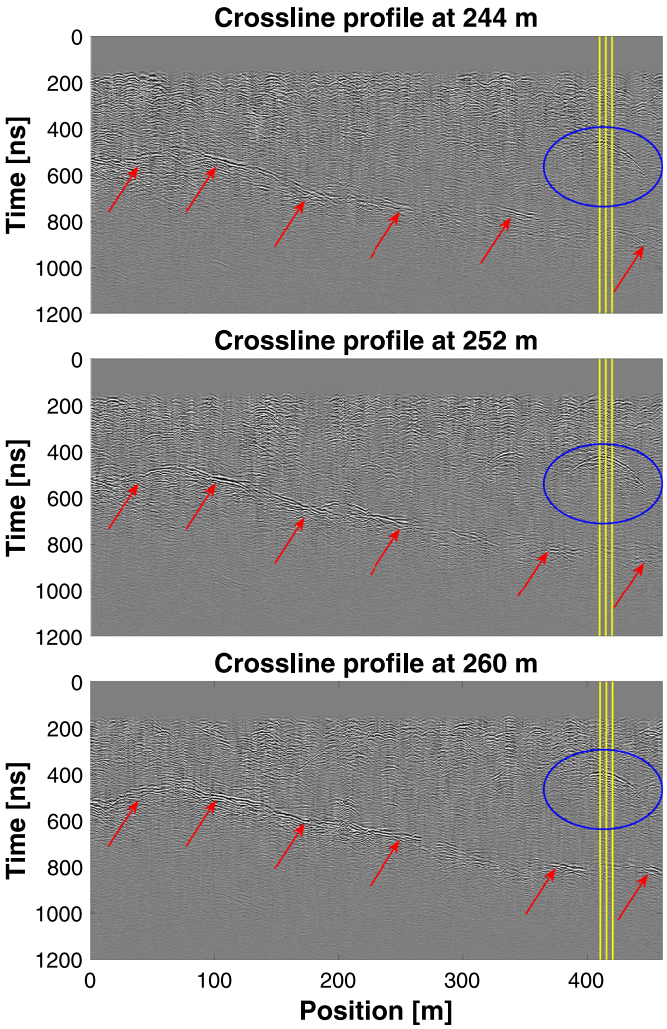

Figure 11. Example crossline GPR profiles. Three profiles separated by 8 m are depicted. Highlighted are the glacier bed (red arrows) and the large englacial feature seen in Figure 10 (blue ellipse). The yellow lines denote the intersections with the three inline profiles shown in Figure 10.

i. Time-zero adjustment based on calibration tests of our system to ensure that the zero time on each GPR trace corresponds with the fire time of the transmitter antenna.
ii. Mean trace removal using a sliding 30-trace window to remove the high-amplitude emitted GPR pulse and associated internal antenna and system ringing, which otherwise tend to overshadow many reflected arrivals.
iii. Minor static adjustment of each trace via Fourier phase shift such that the data conform to a smooth acquisition surface, to reduce vertical 'jumps' in the data and their corresponding horizontal discontinuities, which are caused by small variations in the height of the drone between survey lines.
iv. Relative adjustment of the position of odd- vs even-numbered profiles based on maximizing the correlation between adjacent flight lines in order to correct for the 'acquisition pattern' in the data (Egli and others, 2021a). Indeed, even though the surveyed positions are measured precisely with dGPS, small internal timing delays combined with the flight speed of the drone mean that such a correction is necessary for optimal results.
v. De-wow using a 13-point residual median filter to remove the low-frequency transient upon which the desired GPR reflections from the glacier are superimposed.
vi. Application of a time-varying gain function based on the average observed decay of GPR amplitudes across

https://doi.org/10.1017/jog.2023.83 Published online by Cambridge University Press

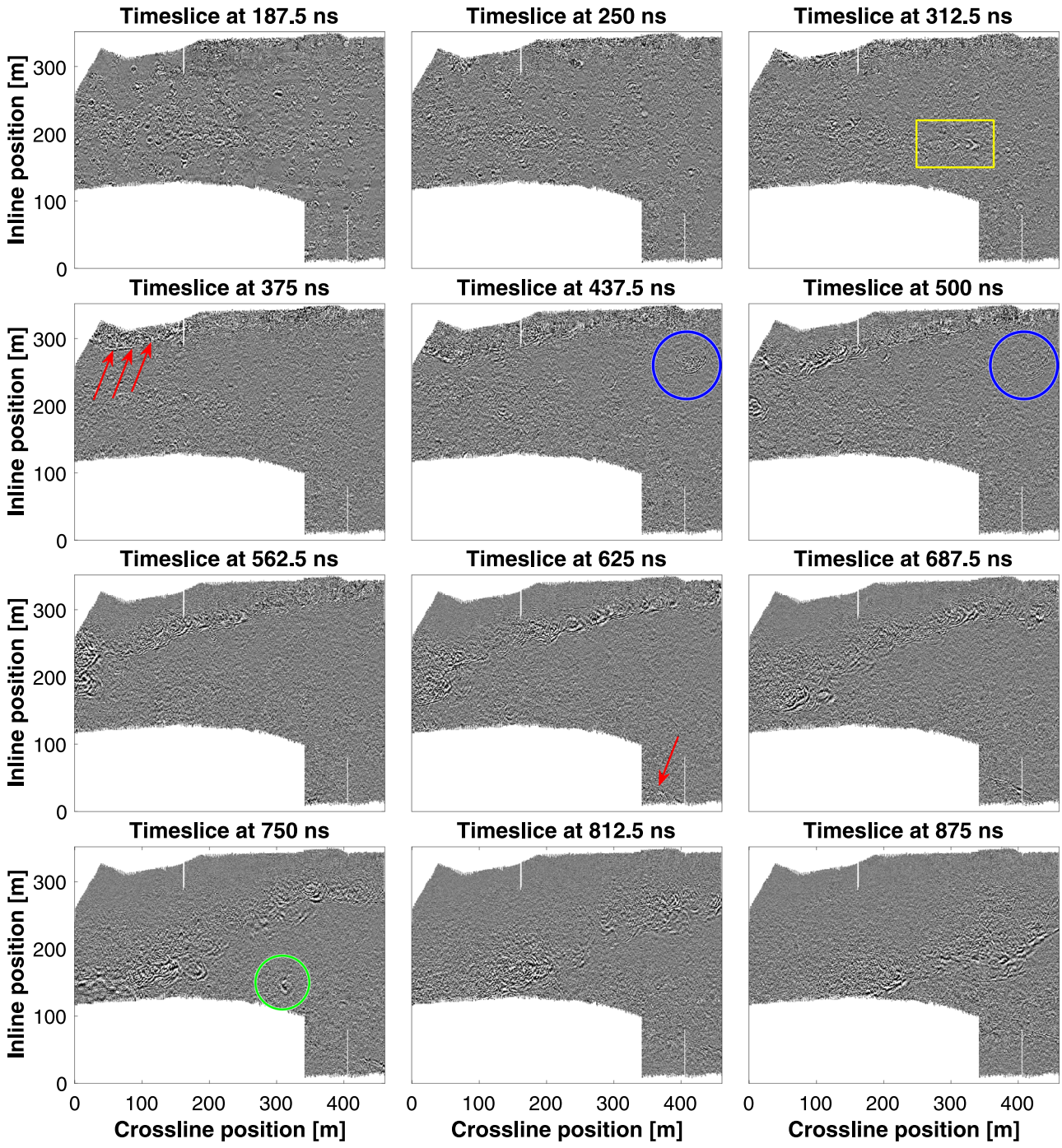

Figure 12. Twelve timeslices from the Otemma 3D GPR dataset taken at regular intervals between 187.5 and 875 ns. The yellow rectangle highlights an elongated englacial feature that is further explored in Figure 13. The red arrows indicate the emergence of the ice-bedrock interface on the northwestern (timeslice at 375 ns) and southeastern (timeslice at 625 ns) sides of the glacier. The blue circles indicate the position of the large englacial feature seen in Figures 10 and 11. The green circle highlights a likely void near the glacier bed.

the dataset, in order to correct for geometrical spreading losses and the effects of signal attenuation. The smoothed inverse of the average amplitude decay curve curve was utilized.

vii. Fourier-transform-based interpolation in time to quadruple the number of points per trace for improved data display and analysis.

4.4. Results

Figures 9–13 present different views of the Otemma dataset after the editing and elementary processing described above. In Figure 9, we show a 3D view of selected intersecting inline and crossline profiles, which are presented in detail in Figures 10 and 11, respectively. We see on all profiles that the interface between the ice and the bedrock is clearly visible, even down to a two-way travel time of 1000 ns. The latter corresponds to a depth of approximately 80 m assuming a radar speed of 0.167 m ns^{-1} in glacier ice (e.g. Plewes and Hubbard, 2001) and considering the 5 m layer of air between the antenna and the ice surface. Numerous internal features are also present, as indicated by the various diffraction hyperbolae that can be seen on the sections, most notably in the upper part of the images but also at depth. These features may represent air voids, water pockets, or large boulders in the ice. As an example, the blue ellipses in Figures 9 and 10 highlight the location of a large hyperbola that can be

https://doi.org/10.1017/jog.2023.83 Published online by Cambridge University Press

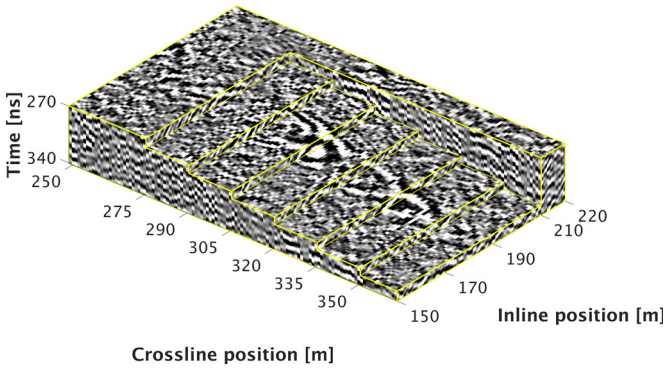

Figure 13. 3D representation of a sub-volume of the Otemma GPR dataset. A large, elongated feature is visible in the crossline direction, extending 80 m horizontally and 60 ns vertically. The location of this feature is marked by a yellow rectangle in Figure 12.

followed over tens of neighboring profiles, which likely represents an air- or water-filled cavity. Tracking the presence of such features in 3D may reveal important and so-far unexplored details about the englacial hydrological system.

In Figure 12, we show twelve timeslices through the Otemma 3D dataset, extracted at regular intervals between 187.5 and 875 ns. In the earliest two panels, multiple circles can be observed whose radii grow in time. Such features represent scattered energy from various heterogeneities within the ice and correspond to the various diffraction hyperbolae seen in Figures 9 and 10. At 312.5 ns, and highlighted with a yellow rectangle, we observe the reflection from a major feature which we believe to be another large englacial channel. Figure 13 presents a detailed 3D view of this feature, where we see that it extends over more than 80 m in the crossline direction and over a time range of approximately 60 ns, clearly dipping in the up-glacier direction. Descending further into the dataset in time, we observe, indicated by the red arrows, the emergence of the glacier bed reflection from the northwestern side of the valley near the top of the timeslice at 375 ns, and another large, englacial feature at 437.5 ns and 500 ns, highlighted with a blue circle. The bedrock reflection from the southeastern side of the valley, indicated by a red arrow, can then be seen to emerge near the bottom of the timeslice at 625 ns, followed by another large internal feature at 750 ns, circled in green, which may correspond to a subglacial feature considering its proximity with the bedrock interface.

5. Discussion and conclusions

The research gap that this study aims to fill is the lack of a suitable data acquisition methodology for recording large, high-density and high-resolution 3D and 4D GPR datasets over alpine glaciers in a safe and efficient manner. Recent studies, as well as the field results presented in this paper, suggest that such data have tremendous potential for revealing detailed information about glacier internal structure and bed conditions, which in turn can be used to better our understanding of alpine glacier hydrology and dynamics. To fill this research need, we have developed a drone-based GPR instrument. Construction of this instrument required bringing together (i) a state-of-the-art GPR controller, custom designed for alpine glacier work, having a long recording time and with real-time sampling to permit thousands of stacks while maintaining a high trace output rate; (ii) a lightweight, 80-MHz, GPR transmit–receive antenna; (iii) a terrain-following navigational system; and (iv) a drone equipped with dGPS positioning. This was followed by elaboration of a clear survey methodology to minimize the risk of a crash during the data acquisition, and optimization of a number of flight parameters to find an acceptable balance between data acquisition speed and data quality. It is important to note that, at the time of writing, at least one commercially available drone-based GPR system for geological applications exists (Malå), and it is expected that more will follow. Although our goal here is not to provide a full comparison with the existing system, we should point out that our developed instrument, specifically intended for glacier acquisitions, has approximately half the payload weight of the commercial system and over three times the trace recording length. The former permits longer survey times and compatibility with a wider variety of drones, whereas the latter allows for greater depths of penetration into the ice when possible.

The key limiting factor of our drone-based GPR system for glaciological work is the drone battery consumption. Under realistic field conditions, we can record approximately 4 line-km of high-quality GPR data on a single set of batteries in approximately 20 min. Maximizing the amount of data that can be acquired in a single day therefore means using multiple sets of batteries and/or bringing a generator or power bank on site, such that charging can occur as the survey is ongoing. For the presented 3D acquisition on the Otemma glacier, a combination of four sets of batteries and a fuel generator were used, which allowed us to record a total of 112 line-km of GPR data in only four field days of moderate intensity. The quality of the resulting 3D data volume is high, with a strong reflection coming from the glacier bed at over 80-m depth, and numerous diffraction hyperbolae being trackable over tens of neighboring profiles, likely indicating the presence of englacial channels. Our current work involves detailed exploration of this Otemma dataset in a glaciological context, as well as the development of advanced data migration and interpretation strategies that are beyond the scope of this work. Multiple 4D datasets have also now been collected with the drone-based GPR system and are currently undergoing analysis.

Acknowledgements. We thank Johanna Klahold and Pascal Egli for their help with field testing of the developed GPR system. We also thank Johanna Klahold, Barthélémy Anhorn, Bruno Galissard de Marignac, Edith Sotelo Gamboa, Floreana Miesen, Frédéric Lardet, Jürg Hunziker, Mélissa Francey, Pau Wiersma and the members of the UNIL AlpWISE group for their help with fieldwork on the Otemma glacier. Thanks also to the team at Utsi Electronics Ltd. for their dedicated support in developing the GPR controller, as well as the team at SPH Engineering for their assistance with the True Terrain Following navigation system. Finally, we thank the two anonymous reviewers as well as associate editor Bernd Kulessa and associate chief editor Hester Jiskoot for comments that greatly helped to improve the quality of the manuscript. This work was supported by a grant to J. Irving from the Swiss National Science Foundation (grant number 200021_188575).

References

Aguasca A, Acevo-Herrera R, Broquetas A, Mallorqui JJ and Fabregas X (2013) ARBRES: light-weight CW/FM SAR sensors for small UAVs. *Sensors* **13**(3), 3204–3216. doi: 10.3390/s130303204.

Arcone SA and Yankielun N (2000) 1.4 GHz radar penetration and evidence of drainage structures in temperate ice: black Rapids Glacier, Alaska. *U.S.A. Journal of Glaciology* **46**(154), 477–490. doi: 10.3189/172756500781833133.

Arcone SA, Lawson DE and Delaney AJ (1995) Short-pulse radar wavelet recovery and resolution of dielectric contrasts within englacial and basal ice of Matanuska Glacier, Alaska, U.S.A. *Journal of Glaciology* **41**(137), 68–86. doi: 10.3189/s0022143000017779.

Bamber JL (1989) Ice/bed interface and englacial properties of Svalbard ice masses deduced from airborne radio echo-sounding data. *Journal of Glaciology* **35**(119), 30–37. doi: 10.3189/002214389793701392.

Bandini F and 6 others (2018) Technical note: bathymetry observations of inland water bodies using a tethered single-beam sonar controlled by an unmanned aerial vehicle. *Hydrology and Earth System Sciences* **22**(8), 4165–4181. doi: 10.5194/hess-22-4165-2018.

Binder D and 5 others (2009) Determination of total ice volume and ice-thickness distribution of two glaciers in the Hohe Tauern region,

Eastern Alps, from GPR data. *Annals of Glaciology* **50**(51), 71–79. doi: 10.3189/172756409789097522.

Bælum K and Benn DI (2011) Thermal structure and drainage system of a small valley glacier (Tellbreen, Svalbard), investigated by ground penetrating radar. *The Cryosphere* **5**, 139–149. doi: 10.5194/tc-5-139-2011.

Booth AD and Koylass TM (2022) Drone-mounted GPR surveying: flight-height considerations for diffraction-based velocity analysis. *Geophysics* **87**(4), WB69–WB79. doi: 10.1190/geo2021-0602.1.

Bradford JH, Nichols J, Mikesell TD and Harper JT (2009) Continuous profiles of electromagnetic wave velocity and water content in glaciers: an example from Bench Glacier, Alaska, USA. *Annals of Glaciology* **50**(51), 1–9. doi: 10.3189/172756409789097540.

Bradford JH, Nichols J, Harper JT and Meierbachtol TW (2013) Compressional and em wave velocity anisotropy in a temperate glacier due to basal crevasses, and implications for water content estimation. *Annals of Glaciology* **54**(64), 168–178. doi: 10.3189/2013AoG64A206.

Brown J, Harper JT and Bradford JH (2009) A radar transparent layer in a temperate valley glacier: Bench Glacier, Alaska. *Earth Surface Processes and Landforms* **34**, 1497–1506. doi: 10.1002/esp.1835.

Burr R and 5 others (2018) Design and Implementation of a FMCW GPR for UAV-based Mine Detection. 2018 IEEE MTT-S International Conference on Microwaves for Intelligent Mobility (ICMIM), 1–4. doi: 10.1109/ICMIM.2018.8443526.

Catapano I and 5 others (2022) Contactless ground penetrating radar imaging: State of the art, challenges, and microwave tomography-based data processing. *IEEE Geoscience and Remote Sensing Magazine* **10**(1), 251–273. doi: 10.1109/MGRS.2021.3082170.

Church G and 5 others (2019) Detecting and characterising an englacial conduit network within a temperate Swiss glacier using active seismic, ground penetrating radar and borehole analysis. *Annals of Glaciology* **60**(79), 193–205. doi: 10.1017/aog.2019.19.

Church G, Grab M, Schmelzbach C, Bauder A and Maurer H (2020) Monitoring the seasonal changes of an englacial conduit network using repeated ground-penetrating radar measurements. *Cryosphere* **14**(10), 3269–3286. doi: 10.5194/tc-14-3269-2020.

Church G, Bauder A, Grab M and Maurer H (2021) Ground-penetrating radar imaging reveals glacier's drainage network in 3D. *Cryosphere* **15**(8), 3975–3988. doi: 10.5194/tc-15-3975-2021.

Del Gobbo C, Colucci RR, Forte E, Triglav Čekada M and Zorn M (2016) The Triglav glacier (South-Eastern Alps, Slovenia): volume estimation, internal characterization and 2000–2013 temporal evolution by means of ground penetrating radar measurements. *Pure and Applied Geophysics* **173**(8), 2753–2766. doi: 10.1007/s00024-016-1348-2.

Dietrich JT (2017) Bathymetric Structure-from-Motion: extracting shallow stream bathymetry from multi-view stereo photogrammetry. *Earth Surface Processes and Landforms* **42**(2), 355–364. doi: 10.1002/esp.4060.

Dill S, Schreiber E, Engel M, Heinzel A and Peichl M (2019) A drone carried multichannel synthetic aperture radar for advanced buried object detection. 2019 IEEE Radar Conference, RadarConf 2019, 1–6. doi: 10.1109/RADAR.2019.8835814.

Døssing A and 6 others (2021) A high-speed, light-weight scalar magnetometer bird for km scale UAV magnetic surveying: on sensor choice, bird design, and quality of output data. *Remote Sensing* **13**(4), 1–24. doi: 10.3390/rs13040649.

Egli PE, Irving J and Lane SN (2021a) Characterization of subglacial marginal channels using 3-D analysis of high-density ground-penetrating radar data. *Journal of Glaciology* **67**(264), 759–772. doi: 10.1017/jog.2021.26.

Egli PE, Belotti B, Ouvry B, Irving J and Lane SN (2021b) Subglacial channels, climate warming, and increasing frequency of alpine glacier snout collapse. *Geophysical Research Letters* **48**(21), 1–11. doi: 10.1029/2021GL096031.

Eisen O, Bauder A, Lüthi M, Riesen P and Funk M (2009) Deducing the thermal structure in the tongue of Gornergletscher, Switzerland, from radar surveys and borehole measurements. *Annals of Glaciology* **50**(51), 63–70. doi: 10.3189/172756409789097612.

ETHZ VAW, EKK/SCNAT (2010) Réseau suisse des observations glaciaires, glacier d'Otemma, Bagnes (VS). Accessed in August 2023. https://web.archive.org/web/20120415054738/http://glaciology.ethz.ch/messnetz/data/otemma.html.

Farinotti D, Huss M, Bauder A, Funk M and Truffer M (2009) A method to estimate the ice volume and ice-thickness distribution of alpine glaciers. *Journal of Glaciology* **55**(191), 422–430. doi: 10.3189/002214309788816759.

Fernandez MG and 6 others (2018) Synthetic aperture radar imaging system for landmine detection using a ground penetrating radar on board a unmanned aerial vehicle. *IEEE Access* **6**(c), 45100–45112. doi: 10.1109/ACCESS.2018.2863572.

Flowers GE and Clarke GKC (1999) Surface and bed topography of Trapridge Glacier, Yukon Territory, Canada: digital elevation models and derived hydraulic geometry. *Journal of Glaciology* **45**(149), 165–174. doi: 10.1017/S0022143000003142.

Fountain AG and Jacobel RW (1997) Advances in ice radar studies of a temperate alpine glacier, South Cascade Glacier, Washington, U.S.A. *Annals of Glaciology* **24**, 303–308. https://doi.org/10.3189/S0260305500012350.

Garambois S, Legchenko A, Vincent C and Thibert E (2016) Ground-penetrating radar and surface nuclear magnetic resonance monitoring of an englacial water-filled cavity in the polythermal glacier of Tête Rousse. *Geophysics* **81**(1), WA131–WA146. doi: 10.1190/geo2015-0125.1.

Glasser NF, Goodsell B, Copland L and Lawson W (2006) Debris characteristics and ice-shelf dynamics in the ablation region of the McMurdo Ice Shelf, Antarctica. *Journal of Glaciology* **52**(177), 223–234. doi: 10.3189/172756506781828692.

Goodsell B, Hambrey MJ and Glasser NF (2002) Formation of band ogives and associated structures at Bas Glacier d'Arolla, Valais, Switzerland. *Journal of Glaciology* **48**(161), 287–300. doi: 10.3189/172756502781831494.

Grab M and 6 others (2018) Ice volume estimates of Swiss glaciers using helicopter-borne GPR - An example from the Glacier de la Plaine Morte. 2018 17th International Conference on Ground Penetrating Radar, GPR 2018, 1–4. doi: 10.1109/ICGPR.2018.8441613.

Grasmueck M, Weger R and Horstmeyer H (2005) Full-resolution 3D GPR imaging. *Geophysics* **70**(1), 12–19. doi: 10.1190/1.1852780.

Harper JT, Bradford JH, Humphrey NF and Meierbachtol TW (2010) Vertical extension of the subglacial drainage system into basal crevasses. *Nature* **467**(7315), 579–582. doi: 10.1038/nature09398.

Harrison CH (1970) Reconstruction of subglacial relief from radio echo sounding records. *Geophysics* **35**(6), 1099–1115. doi: 10.1190/1.1440146.

Irvine-Fynn TDL, Moorman BJ, Williams JLM and Walter FSA (2006) Seasonal changes in ground-penetrating radar signature observed at a polythermal glacier, Bylots Island, Canada. *Earth Surface Processes and Landforms* **31**(7), 892–909. doi: 10.1002/esp.1299.

Jacobel RW and Anderson SK (1987) Interpretation of radio-echo returns from internal water bodies in Variegated Glacier, Alaska, U.S.A. *Journal of Glaciology* **33**(115), 319–323. doi: 10.3189/S002214300000890X.

Jacobel RW and Raymond C (1984) Radio echa-sounding studies of englacial water movement in Variegated Glacier, Alaska. *Journal of Glaciology* **30**(104), 22–29. doi: 10.3189/S0022143000008443.

Jenssen ROR and Jacobsen S (2020) Drone-mounted UWB snow radar: technical improvements and field results. *Journal of Electromagnetic Waves and Applications* **34**(14), 1930–1954. doi: 10.1080/09205071.2020.1799871.

Jenssen ROR, Eckerstorfer M and Jacobsen S (2020) Drone-mounted ultra-wideband radar for retrieval of snowpack properties. *IEEE Transactions on Instrumentation and Measurement* **69**(1), 221–230. doi: 10.1109/TIM.2019.2893043.

King EC, Smith AM, Murray T and Stuart GW (2008) Glacier-bed characteristics of midtre Lovénbreen, Svalbard, from high-resolution seismic and radar surveying. *Journal of Glaciology* **54**(184), 145–156. doi: 10.3189/002214308784409099.

Kolster ME and Døssing A (2021) Simultaneous line shift and source parameter inversion applied to a scalar magnetic survey for small unexploded ordnance. *Near Surface Geophysics* **19**(6), 629–641. doi: 10.1002/nsg.12178.

Kotowski PO and 6 others (2022) Evaluation of a semi-airborne electromagnetic survey based on a multicopter aircraft system. *Geosciences* **12**(1), 26. doi: 10.3390/geosciences12010026.

Koutalakis P and Zaimes GN (2022) River flow measurements utilizing UAV-based surface velocimetry and bathymetry coupled with sonar. *Hydrology* **9**(8), 148. doi: 10.3390/hydrology9080148.

Kulessa B, Booth AD, Hobbs A and Hubbard AL (2008) Automated monitoring of subglacial hydrological processes with ground-penetrating radar (GPR) at high temporal resolution: scope and potential pitfalls. *Geophysical Research Letters* **35**(24), 1–5. doi: 10.1029/2008GL035855.

Kunze C and 5 others (2022) Development of a UAV-based gamma spectrometry system for natural radionuclides and field tests at central Asian uranium legacy sites. *Remote Sensing* **14**(9), 2147. doi: 10.3390/rs14092147.

Kurowski M, Thal J, Damerius R, Korte H and Jeinsch T (2019) Automated survey in very shallow water using an unmanned surface vehicle. *IFAC-PapersOnLine* **52**(21), 146–151. doi: 10.1016/j.ifacol.2019.12.298.

Langhammer L, Rabenstein L, Bauder A and Maurer HR (2017) Ground-penetrating radar antenna orientation effects on temperate mountain glaciers. *Geophysics* **82**(3), H15–H24. doi: 10.1190/GEO2016-0341.1.

Langhammer L and 6 others (2019a) Glacier bed surveying with helicopter-borne dual-polarization ground-penetrating radar. *Journal of Glaciology* **65**(249), 123–135. doi: 10.1017/jog.2018.99.

Langhammer L, Grab M, Bauder A and Maurer HR (2019b) Glacier thickness estimations of alpine glaciers using data and modeling constraints. *The Cryosphere* **13**(8), 2189–2202. doi: 10.5194/tc-13-2189-2019.

Lehmann F, Boerner DE, Holliger K and Green AG (2000) Multicomponent georadar data: some important implications for data acquisition and processing. *Geophysics* **65**(5), 1542–1552. doi: 10.1190/1.1444842.

Lin YC and 7 others (2019) Evaluation of UAV LiDAR for mapping coastal environments. *Remote Sensing* **11**(24), 1–32. doi: 10.3390/rs11242893.

Luo K and 7 others (2022) First unmanned aerial vehicle airborne gravimetry based on the CH-4 UAV in China. *Journal of Applied Geophysics* **206**, 104835. doi: 10.1016/j.jappgeo.2022.104835.

Malå. Airborne Ground Penetrating Radar System. Accessed in September 2023. https://www.guidelinegeo.com/product/mala-geodrone/.

Merz K, Green AG, Buchli T, Springman SM and Maurer H (2015) A new 3-D thin-skinned rock glacier model based on helicopter GPR results from the Swiss Alps. *Geophysical Research Letters* **42**(11), 4464–4472. doi: 10.1002/2015GL063951.

Mingo L, Flowers GE, Crawford AJ, Mueller DR and Bigelow DG (2020) A stationary impulse-radar system for autonomous deployment in cold and temperate environments. *Annals of Glaciology* **61**(81), 99–107. doi: 10.1017/aog.2020.2.

Moorman BJ and Michel FA (2000) Glacial hydrological system characterization using ground-penetrating radar. *Hydrological Processes* **14**, 2656–2667. doi: 10.1002/1099-1085(20001030)14:15<2645::AID-HYP84>3.0.CO;2-2.

Murray T and 6 others (2000) Glacier surge propagation by thermal evolution at the bed. *Journal of Geophysical Research: Solid Earth* **105**(B6), 13491–13507. doi: 10.1029/2000jb900066.

Murray T, Booth AD and Rippin DM (2007) Water-Content of Glacier-Ice: limitations on estimates from velocity analysis of SUrface ground-penetration radar surveys. *Journal of Environmental and Engineering Geophysics* **12**, 87–99. doi: 10.2113/JEEG12.1.87.

NPOC. Contains modified Copernicus Sentinel data (2020) swisstopo/NPOC. Swiss National Point of Contact for Satellite Images. Accessed in September 2023. https://www.npoc.ch/en/services/products.html.

Narod B and Clarke G (1994) Miniature high-power impulse transmitter for radio-echo sounding. *Journal of Glaciology* **40**(134), 190–194. doi: 10.3189/S002214300000397X.

Nobes DC, Davis EF and Arcone SA (2005) "Mirror-image" multiples in ground-penetrating radar. *Geophysics* **70**(1), 20–22. doi: 10.1190/1.1852781.

Parshin A and 7 others (2021) Lightweight unmanned aerial system for time-domain electromagnetic prospecting-the next stage in applied UAV-geophysics. *Applied Sciences (Switzerland)* **11**(5), 1–26. doi: 10.3390/app11052060.

Pettersson R, Jansson P and Blatter H (2004) Spatial variability in water content at the cold-temperate transition surface of the polythermal Storglaciären, Sweden. *Journal of Geophysical Research: Earth Surface* **109** (F02009), 1–12. doi: 10.1029/2003jf000110.

Plewes LA and Hubbard B (2001) A review of the use of radio-echo sounding in glaciology. *Progress in Physical Geography: Earth and Environment* **25**(2), 203–236. doi: 10.1177/030913330102500203.

Remy MA, de Macedo KAC and Moreira JR (2012) The first UAV-based P- and X-band interferometric SAR system. IEEE International Geoscience and Remote Sensing Symposium, 5041–5044. doi: 10.1109/IGARSS.2012.6352478.

Rutishauser A, Maurer HR and Bauder A (2016) Helicopter-borne ground-penetrating radar investigations on temperate alpine glaciers: a comparison of different systems and their abilities for bedrock mapping. *Geophysics* **81** (1), WA119–WA129. doi: 10.1190/GEO2015-0144.1.

Rutishauser A and 7 others (2022) Radar sounding survey over Devon Ice Cap indicates the potential for a diverse hypersaline subglacial hydrological environment. *Cryosphere* **16**(2), 379–395. doi: 10.5194/tc-16-379-2022.

Saintenoy A and 6 others (2011) High density coverage investigation of the Austre LovénBreen (Svalbard) using Ground Penetrating Radar. 2011 6th International Workshop on Advanced Ground Penetrating Radar, IWAGPR 2011, 11–14. doi: 10.1109/IWAGPR.2011.5963894.

Saintenoy A and 7 others (2013) Deriving ice thickness, glacier volume and bedrock morphology of Austre Lovénbreen (Svalbard) using GPR. *Near Surface Geophysics* **11**(2), 253–261. doi: 10.3997/1873-0604.2012040.

Schroeder DM (2022) Paths forward in radioglaciology. *Annals of Glaciology* **63**(87-89), 13–17. doi: 10.1017/aog.2023.3.

Schroeder DM and 9 others (2020) Five decades of radioglaciology. *Annals of Glaciology* **61**(81), 1–13. doi: 10.1017/aog.2020.11.

Sharp M and 6 others (1993) Geometry, bed topography and drainage system structure of the haut glacier d'Arolla, Switzerland. *Earth Surface Processes and Landforms* **18**, 557–571. doi: 10.1002/esp.3290180608.

SPH Engineering. Using a drone based ground-penetrating radar for avalanche victim search: a study case from northern Spain. Accessed in August 2023. https://www.sphengineering.com/news/using-a-drone-based-ground-penetrating-radar-for-avalanche-victim-search-a-case-study-from-northern-spain.

Stoll JB and 7 others (2019) Semi-Airborne electromagnetics using a multicopter. In International Workshop on Gravity, Electrical & Magnetic Methods and Their Applications, Xi'an, China, 19-22 May 2019 (pp. 363–366). Society of Exploration Geophysicists and Chinese Geophysical Society. doi: 10.1190/GEM2019-092.1.

Swisstopo. Map of Switzerland. Federal Office of Topography. Accessed in August 2023. https://map.geo.admin.ch.

Tao P and 6 others (2022) Recognition of ecological vegetation fairy circles in intertidal salt marshes from UAV LiDAR point clouds. *International Journal of Applied Earth Observation and Geoinformation* **114**(April), 103029. doi: 10.1016/j.jag.2022.103029.

Urbini S and 7 others (2017) Airborne radio echo sounding (RES) measures on alpine glaciers to evaluate ice thickness and bedrock geometry: preliminary results from pilot tests performed in the ortles-cevedale group (Italian Alps). *Annals of Geophysics* **60**(2), 1–12. doi: 10.4401/ag-7122.

Valence E, Baraer M, Rosa E, Barbecot F and Monty C (2022) Drone-based ground-penetrating radar (GPR) application to snow hydrology. *Cryosphere* **16**(9), 3843–3860. doi: 10.5194/tc-16-3843-2022.

van der Veeke S and 5 others (2021a) Footprint and height corrections for UAV-borne gamma-ray spectrometry studies. *Journal of Environmental Radioactivity* **231**, 106545. doi: 10.1016/j.jenvrad.2021.106545.

van der Veeke S, Limburg J, Koomans RL, Söderström M and van der Graaf ER (2021b) Optimizing gamma-ray spectrometers for UAV-borne surveys with geophysical applications. *Journal of Environmental Radioactivity* **237**, 106717. doi: 10.1016/j.jenvrad.2021.106717.

Vincent C and 5 others (2012) Detection of a subglacial lake in Glacier de Tête Rousse (Mont Blanc area, France). *Journal of Glaciology* **58**(211), 866–878. doi: 10.3189/2012JoG11J179.

Walter C, Braun A and Fotopoulos G (2021) Characterizing electromagnetic interference signals for unmanned aerial vehicle geophysical surveys. *Geophysics* **86**(6), J21–J32. doi: 10.1190/geo2020-0895.1.

Weiner S and 6 others (2020) A Flight Capable Atomic Gravity Gradiometer With a Single Laser. INERTIAL 2020 - 7th IEEE International Symposium on Inertial Sensors and Systems, Proceedings, 31–33. doi: 10.1109/INERTIAL48129.2020.9090014.

Weiss M and Ender G (2005) A 3D imaging radar for small unmanned airplanes - ARTINO. European Radar Conference EURAD 2005, 209–212. doi: 10.1109/EURAD.2005.1605602.

Woodward J, Murray T, Clark RA and Stuart GW (2003) Glacier surge mechanisms inferred from ground-penetrating radar: Kongsvegen, Svalbard. *Journal of Glaciology* **49**(167), 473–480. doi: 10.3189/172756503781830458.

Wu K and 6 others (2019) A new drone-borne GPR for soil moisture mapping. *Remote Sensing of Environment*, **235**, 111456. doi: 10.1016/j.rse.2019.111456.

Yarleque MA, Alvarez S and Martinez HJ (2017) FMCW GPR radar mounted in a mini-UAV for archaeological applications: First analytical and measurement results. Proceedings of the 2017 19th International Conference on Electromagnetics in Advanced Applications, ICEAA 2017, 1646–1648. doi: 10.1109/ICEAA.2017.8065606.

Yin D and Wang L (2019) Individual mangrove tree measurement using UAV-based LiDAR data: possibilities and challenges. *Remote Sensing of Environment* **223**, 34–49. doi: 10.1016/j.rse.2018.12.034.

Zaugg E and 8 others (2010) Using the MicroASAR on the NASA SIERRA UAS in the Characterization of Arctic Sea Ice Experiment. IEEE National Radar Conference - Proceedings, 271–276. doi: 10.1109/RADAR.2010.5494611.

https://doi.org/10.1017/jog.2023.83 Published online by Cambridge University Press